Featured in Physics

Dirac Surface States in Intrinsic Magnetic Topological Insulators EuSn$_2$As$_2$ and MnBi$_{2n}$Te$_{3n+1}$

Hang Li [1,2,§] Shun-Ye Gao, [1,2,§] Shao-Feng Duan, [3,§] Yuan-Feng Xu, [1,4,§] Ke-Jia Zhu, [1,2,§] Shang-Jie Tian [5,§] Jia-Cheng Gao, [1,2] Wen-Hui Fan, [1,2] Zhi-Cheng Rao [1,2] Jie-Rui Huang, [1,2] Jia-Jun Li, [1,2] Da-Yu Yan, [1,2] Zheng-Tai Liu, [6] Wan-Ling Liu, [6] Yao-Bo Huang, [7] Yu-Liang Li, [8] Yi Liu, [8] Guo-Bin Zhang, [8] Peng Zhang, [9] Takeshi Kondo, [9,10] Shik Shin, [9,10] He-Chang Lei, [5] You-Guo Shi, [1,11] Wen-Tao Zhang, [3,*] Hong-Ming Weng [1,2,11,†] Tian Qian [1,11,‡] and Hong Ding [1,2,11,12]

[1]*Beijing National Laboratory for Condensed Matter Physics and Institute of Physics, Chinese Academy of Sciences, Beijing 100190, China*
[2]*University of Chinese Academy of Sciences, Beijing 100049, China*
[3]*Key Laboratory of Artificial Structures and Quantum Control (Ministry of Education), Shenyang National Laboratory for Materials Science, School of Physics and Astronomy, Shanghai Jiao Tong University, Shanghai 200240, China*
[4]*Max Planck Institute of Microstructure Physics, Halle 06120, Germany*
[5]*Department of Physics and Beijing Key Laboratory of Opto-electronic Functional Materials and Micro-nano Devices, Renmin University of China, Beijing 100872, China*
[6]*State Key Laboratory of Functional Materials for Informatics, Shanghai Institute of Microsystem and Information Technology (SIMIT), Chinese Academy of Sciences, Shanghai 200050, China*
[7]*Shanghai Synchrotron Radiation Facility, Shanghai Advanced Research Institute, Chinese Academy of Sciences, 201204 Shanghai, China*
[8]*National Synchrotron Radiation Laboratory, University of Science and Technology of China, Hefei 230029, China*
[9]*Institute for Solid State Physics, University of Tokyo, Kashiwa, Chiba 277-8581, Japan*
[10]*AIST-UTokyo Advanced Operando-Measurement Technology Open Innovation Laboratory (OPERANDO-OIL), Kashiwa, Chiba 277-8581, Japan*
[11]*Songshan Lake Materials Laboratory, Dongguan, Guangdong 523808, China*
[12]*CAS Center for Excellence in Topological Quantum Computation, University of Chinese Academy of Sciences, Beijing 100049, China*

In magnetic topological insulators (TIs), the interplay between magnetic order and nontrivial topology can induce fascinating topological quantum phenomena, such as the quantum anomalous Hall effect, chiral Majorana fermions, and axion electrodynamics. Recently, a great deal of attention has been focused on the intrinsic magnetic TIs, where disorder effects can be eliminated to a large extent, which is expected to facilitate the emergence of topological quantum phenomena. Despite intensive efforts, experimental evidence of the topological surface states (SSs) remains elusive. Here, by combining first-principles calculations and angle-resolved photoemission spectroscopy (ARPES) experiments, we reveal that EuSn$_2$As$_2$ is an antiferromagnetic TI with the observation of Dirac SSs consistent with our prediction. We also observe nearly gapless Dirac SSs in antiferromagnetic TIs MnBi$_{2n}$Te$_{3n+1}$ ($n = 1$ and 2), which are absent in previous ARPES results. These results provide clear evidence for nontrivial topology of these intrinsic magnetic TIs. Furthermore, we find that the topological SSs show no observable changes across the magnetic transition within the experimental resolution, indicating that the magnetic order has a quite small effect on the topological SSs, which can be attributed to weak hybridization between the localized

magnetic moments, from either $4f$ or $3d$ orbitals, and the topological electronic states. This finding provides insights for further research that the correlations between magnetism and topological states need to be strengthened to induce larger gaps in the topological SSs, which will facilitate the realization of topological quantum phenomena at higher temperatures.

Subject Areas: Condensed Matter Physics,
Topological Insulators

I. INTRODUCTION

Time-reversal symmetry plays a key role in topological quantum states of matter. The earliest discovered topological insulator (TI), the Chern insulator with the integer quantum Hall effect, requires breaking the time-reversal symmetry [1–3]. The thinking and research on time-reversal symmetry in condensed matter systems directly led to the discovery of time-reversal-invariant (TRI) Z_2 TIs with the quantum spin Hall effect [4–7]. The introduction of magnetism into the Z_2 TIs can produce more exotic topological quantum phenomena, such as the quantum anomalous Hall effect [8–14], axion insulator states [15–21], and chiral Majorana fermions [22].

The quantum anomalous Hall effect was first realized in magnetically doped $(Bi, Sb)_2Te_3$ thin films [9,10]. In magnetically doped TIs, the magnetic impurities usually introduce strong inhomogeneity, which is believed to be one of the main reasons that the quantum anomalous Hall effect usually appears at extremely low temperatures (<100 mK), hindering further exploration of topological quantum effects. A direct solution to avoid disorder is to seek for intrinsic magnetic TIs, which have magnetic order in the stoichiometric compositions.

In the past year, significant progress has been made in this field [16–21,23–39]. Theory predicts several intrinsic antiferromagnetic (AFM) TIs, such as $MnBi_2Te_4$ [16, 19–21,33,40] and $EuIn_2As_2$ [17], while most experimental studies focus on $MnBi_2Te_4$ [18,21,25–27,30–39]. Very recently, a quantized Hall plateau at h/e^2 was realized in few-layer $MnBi_2Te_4$ sheets under moderate magnetic fields of several Tesla [30,32]. The intriguing phenomenon is attributed to the transition from an AFM TI to a Chern insulator driven by magnetic fields. Angle-resolved photoemission spectroscopy (ARPES) experiments on $MnBi_2Te_4$ and $MnBi_4Te_7$ reveal a large gap of approximately 100 meV in the AFM phase, which is considered to be associated with the time-reversal-symmetry breaking [21,25–29]. However, it is confusing that the large gap remains when the time-reversal symmetry is restored at temperatures much higher than the AFM transition temperature (T_N) [21,25–29]. Another ARPES experiment on $EuSn_2P_2$ did not obtain information about the topological surface states (SSs), because the samples were hole doped with the bulk band gap above the Fermi level (E_F) [24].

In this work, we not only reveal the Dirac SSs of $MnBi_2Te_4$ and $MnBi_4Te_7$ within the large gap observed in previous ARPES studies, but also discover another intrinsic magnetic TI $EuSn_2As_2$ by combining first-principles calculations and ARPES measurements. Through a systematic study of these magnetic TIs, we obtain a comprehensive picture that, while the magnetic order plays an important role in time-reversal-symmetry breaking, the coupling strength between the local magnetic moments and the topological electronic states is critical for the size of the opened gap in the topological SSs.

II. RESULTS

$EuSn_2As_2$ has a layered crystal structure with space group R-$3m$ [Fig. 1(a)]. Each trigonal Eu layer is sandwiched between two buckled honeycomb SnAs layers. Two adjacent SnAs layers are coupled by the van der Waals force. This coupling allows $EuSn_2As_2$ to be easily exfoliated into few-layer sheets like $MnBi_2Te_4$ [26,30–32,41]. A previous study reveals that $EuSn_2As_2$ undergoes a transition from a paramagnetic (PM) phase to an AFM phase around 25 K [41], which is consistent with our measurements in Figs. 1(b) and 1(c). In the AFM phase, the Eu $4f$ magnetic moments form an A-type AFM structure, i.e., ferromagnetic a-b planes coupled antiferromagnetically along the c axis. In addition, when the magnetic fields are perpendicular to the c axis, the susceptibility $\chi(T)$ in Fig. 1(b) shows an upturn below 10 K, and the isothermal magnetization $M(H)$ at 2 K in Fig. 1(c) increases rapidly at low fields, indicating an in-plane ferromagnetic component probably due to canting of the magnetic moments.

We first analyze the topological properties of $EuSn_2As_2$ in the PM phase. We treat the Eu $4f$ states as core states in the pseudopotential band calculations of the PM phase in Fig. 1(e), since the localized Eu $4f$ states are located at approximately 1.7 eV below E_F [Fig. 2(a)] and have negligible coupling with the other bands near E_F. The calculated bands show a continuous gap throughout the Brillouin zone (BZ) near E_F. For three-dimensional insulators with both inversion and time-reversal symmetries, one can use the Fu-Kane formula to compute the Z_2 invariant based on the parity eigenvalues at the eight TRI points in the BZ [42]. The numbers of occupied bands of odd parity at the eight TRI points are listed in Table I. The obtained invariant $Z_2 = 1$ indicates that $EuSn_2As_2$ is a strong TI in the PM phase.

In the band calculations of the AFM phase in Fig. 1(f), we consider two metastable AFM phases with the magnetic moments along the b (AFM-b) and c (AFM-c) axes, respectively. The Hubbard interaction U on the Eu $4f$

electrons is set to be 5 eV, in order to make the energy position of the Eu $4f$ bands consistent with the experimental results in Fig. 2(a). In the AFM configuration, the pseudopotential of Eu must treat the $4f$ states as valence states. The calculated bands of the two AFM phases are almost identical. The continuous gap throughout the BZ remains in the AFM phases. In both AFM phases of $EuSn_2As_2$, the time-reversal symmetry is broken and the inversion symmetry is preserved. One can compute the Z_4 invariant based on the parity eigenvalues at the eight TRI points. The numbers of occupied bands of odd parity at the eight TRI points are listed in Table I. The obtained invariant $Z_4 = 2$ indicates that $EuSn_2As_2$ is an axion insulator in the AFM phase regardless of the spin orientations.

Based on the above analysis, $EuSn_2As_2$ transforms from a strong TI in the PM phase to an axion insulator in the AFM phase below T_N. The effects of the topological phase transition on the Dirac SSs depend on the magnetic structures, spin orientations, and sample surfaces. Here, we consider the SSs on the (001) surface in the AFM-b and AFM-c phases. The analysis is similar to that for $EuIn_2As_2$ [17]. In both phases, the $\mathcal{T}\ell_{1/2}$ symmetry is broken at the (001) surface, where-$\mathcal{T}$ is the time-reversal symmetry and $\ell_{1/2}$ is a translation operation of half of the magnetic unit cell along the c axis, as indicated in Fig. 1(a). The breaking of $\mathcal{T}\ell_{1/2}$ symmetry causes the Dirac SSs to open an energy gap at $\bar{\Gamma}$. However, in the AFM-b phase, the vertical mirror symmetry (M_y) perpendicular to the magnetic moments is
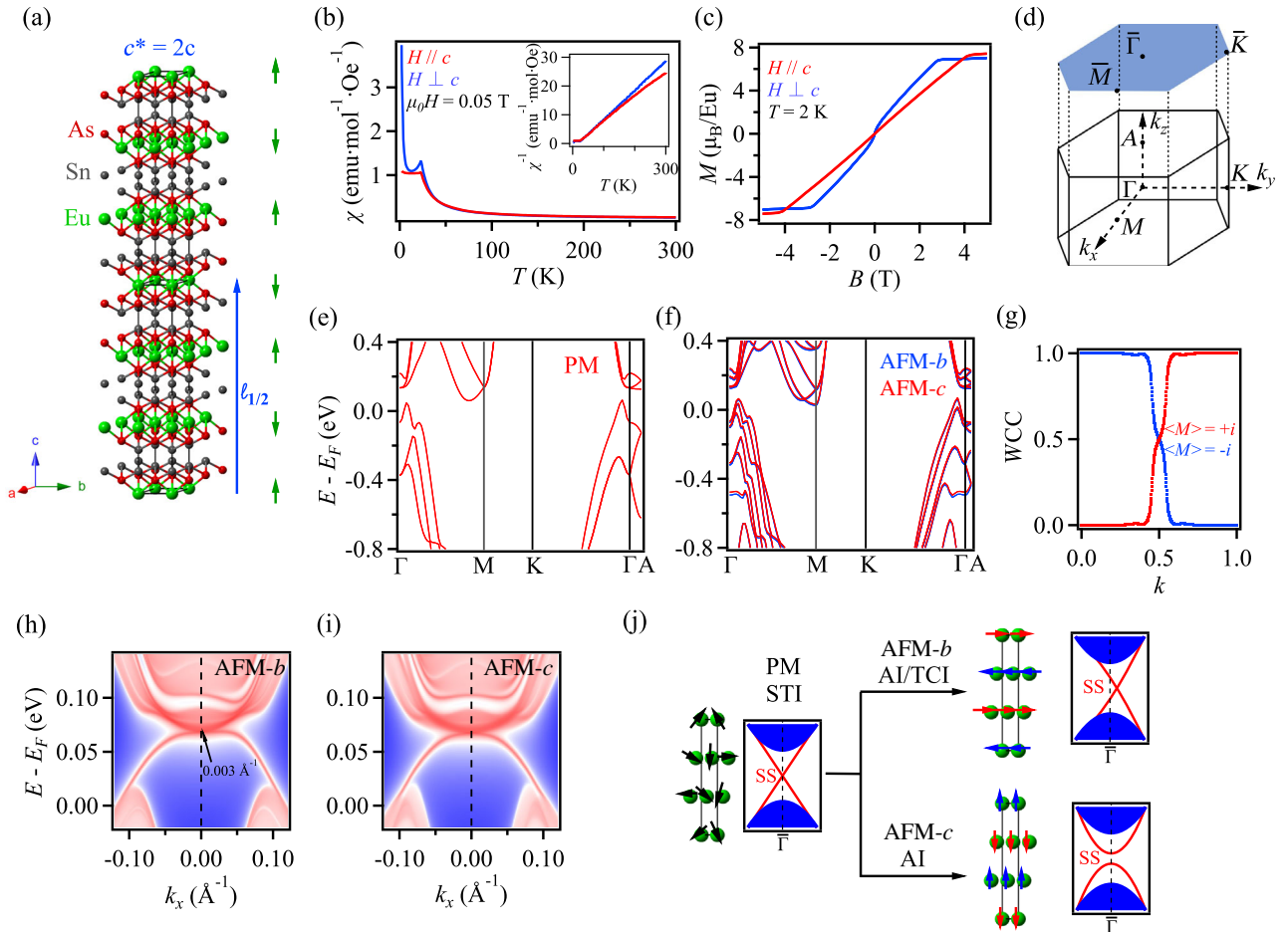

FIG. 1. Magnetic and topological properties of $EuSn_2As_2$. (a) Crystal structure of $EuSn_2As_2$. The green arrows represent the magnetic moments of Eu atoms, forming a doubled magnetic unit cell $c* = 2c$ in the AFM phase. The blue arrow represents the half translation operator $\ell_{1/2}$ of the magnetic unit cell along the c axis. (b) Temperature dependence of magnetic susceptibility $\chi(T)$ with magnetic field $\mu_0H = 0.05$ T parallel (red line) and perpendicular (blue line) to the c axis. The inset shows the inverse susceptibility. (c) Field-dependent magnetization at 2 K with magnetic fields parallel (red line) or perpendicular (blue line) to the c axis. (d) Bulk BZ and (001) surface BZ. k_y and k_z are along the b and c axes, respectively. (e),(f) Calculated bulk band structures of $EuSn_2As_2$ in the PM and AFM-b/AFM-c phases along high-symmetry lines with spin-orbit coupling. (g) Wannier charge centers (WCC) calculated for the occupied bands with mirror eigenvalue $\langle M \rangle = +i$ $(-i)$ in the mirror plane $k_y = 0$. (h),(i) Calculated band dispersions of the (001) SSs and projected bulk states along $\bar{\Gamma}$-$\bar{M}$ near the bulk band gap in the AFM-b and AFM-c phases. (j) Schematic diagram of the topological states of $EuSn_2As_2$ in three prototypical magnetic phases (PM, AFM-b, and AFM-c). STI, TCI, and AI are the abbreviations for strong topological insulator, topological crystalline insulator, and axion insulator, respectively.
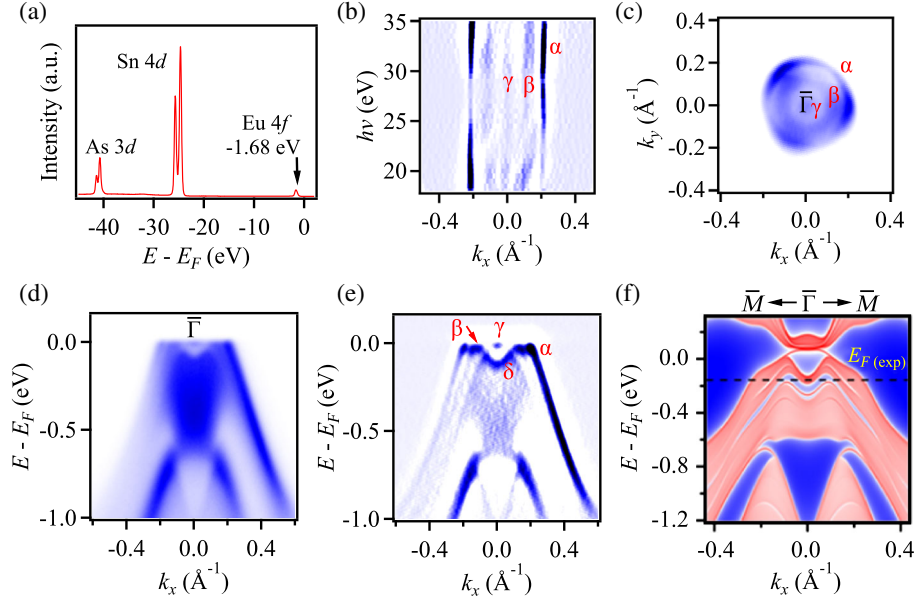
FIG. 2.   Electronic structures below E_F of EuSn$_2$As$_2$. (a) Core-level photoemission spectrum showing the characteristic peaks of As $3d$, Sn $4d$, and Eu $4f$ orbitals. (b) Curvature intensity map of the ARPES data at E_F along $\bar{\Gamma}$-$\bar{M}$ taken in a range of $h\nu$ from 18 to 35 eV. (c) ARPES intensity map at E_F around $\bar{\Gamma}$. (d) ARPES intensity map along $\bar{\Gamma}$-$\bar{M}$. (e) Curvature intensity map of the data in (d). (f) Calculated band dispersions of the (001) SSs and projected bulk states along $\bar{\Gamma}$-$\bar{M}$. The ARPES data in (c) and (d) are collected at $h\nu = 29$ eV. All ARPES data in this figure are collected at 50 K.

preserved and can protect gapless Dirac SSs away from $\bar{\Gamma}$ on the (001) surface. Our calculations in Fig. 1(g) show that the $k_y = 0$ plane has a nonzero mirror Chern number $n_{M_y=\pm i} = \mp 1$, indicating that EuSn$_2$As$_2$ is also a topological crystalline insulator in the AFM-b phase. The nonzero mirror Chern number protects a gapless Dirac cone on the $k_y = 0$ line on the (001) surface. As seen in Fig. 1(h), the calculated Dirac point is located 0.003 Å^{-1} deviating from $\bar{\Gamma}$ on the $k_y = 0$ line. In the AFM-c phase, all vertical mirror symmetries are broken, since the magnetic moments are parallel to them, leaving gapped Dirac SSs on the (001) surface. Note that the opened gap at $\bar{\Gamma}$ is too small (<1 meV) to be resolved in the calculations in Fig. 1(i). The above analysis is illustrated in the schematic diagram in Fig. 1(j).

We then investigate the electronic structures on the (001) surface of EuSn$_2$As$_2$ with ARPES measurements. The electronic structures measured at different photon energies ($h\nu$) in Fig. 2(b) have no obvious changes. We use the data collected with $h\nu = 29$ eV to illustrate the electronic structures near E_F in the PM phase in Figs. 2(c)–2(e).

The data reveal that all near-E_F bands lie around the BZ center $\bar{\Gamma}$. Two holelike bands (labeled as α and β) form two circular FSs centered at $\bar{\Gamma}$. In addition, one can see a small feature at E_F at $\bar{\Gamma}$ (labeled as γ), which should be the bottom of an electronlike band, and an "M"-shaped band below E_F (labeled as δ). The experimental data are consistent with the calculated valence bands in Fig. 2(f) except for a rigid band shift of approximately 0.18 eV. This result suggests that the EuSn$_2$As$_2$ samples are hole doped, which is similar to the case of EuSn$_2$P$_2$ [24].

For the hole-doped samples, conventional ARPES measurements cannot obtain the information in the band gap. Instead, we use time-resolved ARPES (tr-ARPES) with the pump-probe method to measure the unoccupied electronic states above E_F. In Fig. 3(a), the snapshots of ARPES intensity at different pump-probe delay times reveal Dirac-like band dispersions at approximately 0.4 eV above E_F. To illustrate the topological properties of the Dirac band, we combine the tr-ARPES data with the conventional ARPES data in Fig. 3(d). The lower branch of the Dirac band connects to the band α. The bands β and γ connect just above E_F and constitute a single band with an M shape.

TABLE I.   Numbers of occupied bands of odd parity at the eight TRI points in the PM and AFM-b/AFM-c phases of EuSn$_2$As$_2$, respectively.

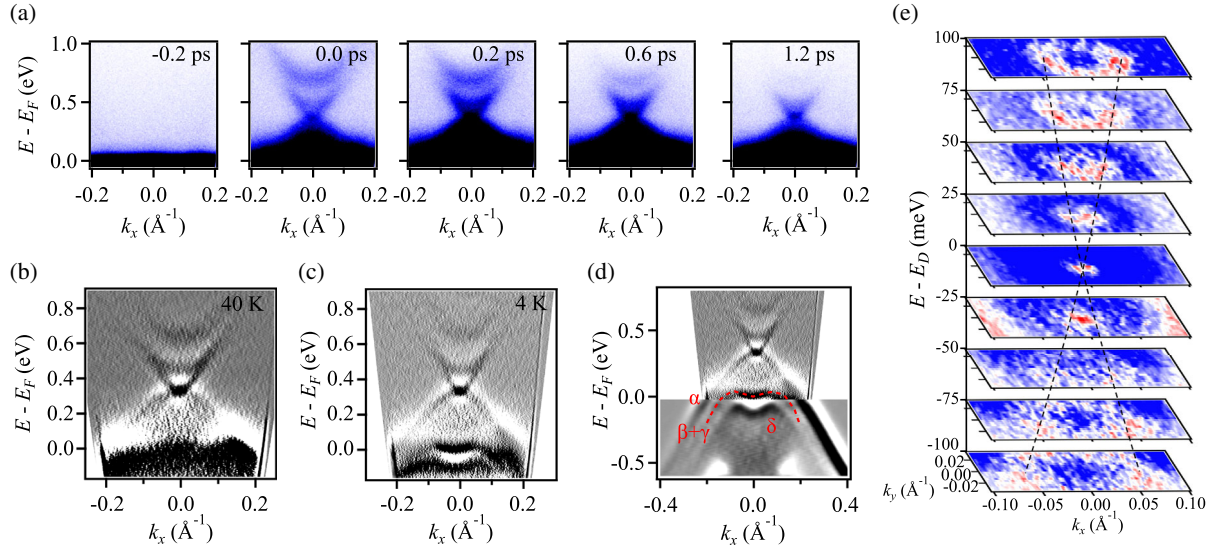| TRIM	$(0, 0, 0)$	$(\pi, 0, 0)$	$(0, \pi, 0)$	$(\pi, \pi, 0)$	$(0, 0, \pi)$	$(\pi, 0, \pi)$	$(0, \pi, \pi)$	(π, π, π)
PM	100	102	102	102	102	102	102	102
AFM-b/c	230	232	232	232	225	225	225	225

FIG. 3. Dirac SSs above E_F on the (001) surface of EuSn$_2$As$_2$. (a) Snapshots of the tr-ARPES intensity along $\bar{\Gamma}$-$\bar{M}$ taken with the pump-probe method at different delay times. (b),(c) Curvature intensity maps of the pump-probe data at the delay time 0.2 ps taken at 40 and 4 K. (d) Combination of the data in Figs. 3(c) and 2(e). (e) Stack of curvature intensity maps of the pump-probe data at different constant energies. The energy of the Dirac point (E_D) is set to zero.

The upper branch of the Dirac band connects to the electronlike conduction band. It is expected that the development of long-range AFM order with an A-type magnetic structure leads to band folding along k_z and band reconstruction. We do not identify the effects in the bulk electronic structures because of the low spectral intensity of the tr-ARPES data. The stack of equal-energy contours in Fig. 3(e) shows that the Dirac SSs has a conelike feature, which is rather isotropic. Compared with the experimental results, the Dirac point in the calculated SSs in Figs. 1(h) and 1(i) is closer to the conduction bands. The discrepancy is attributed to the difference in the surface conditions, which can change the band dispersions of SSs but does not change the topological properties.

The observation of a single Dirac cone across the bulk band gap is consistent with our theoretical predication that EuSn$_2$As$_2$ is a strong TI in the PM phase. As discussed above, the (001) Dirac SSs either open an energy gap or shift slightly off the $\bar{\Gamma}$ point in the AFM phase. Within our resolution, we do not observe any significant changes in the Dirac SSs between the PM and AFM phases. According to our calculations, the effect of the magnetic order on the Dirac SSs is very limited. The main reason is that the coupling between the electronic states involved in the magnetic order and those in the nontrivial topology are too weak. The magnetic moments derive from the Eu $4f$ states, which are very localized and lie at 1.7 eV below E_F. The nontrivial topology is caused by the inversion of the Sn $5p$ and As $4p$ states near E_F. In the AFM phase, the Eu $4f$ magnetic moments form a long-range order, which breaks the time-reversal symmetry, allowing the surface Dirac bands to hybridize and develop an energy gap at $\bar{\Gamma}$.

The magnitude of hybridization depends on the hopping probability between the Eu $4f$ states and the p orbitals related to the nontrivial topology. Since the topological electronic states have little contribution from the Eu $4f$ states, the effects of magnetic order on the Dirac SSs are very limited.

We have revealed that EuSn$_2$As$_2$ is a magnetic TI with no observable gap in the Dirac SSs. The behavior seems to be significantly different from the large gap of tens of meV predicted in another widely studied magnetic TI family, MnBi$_{2n}$Te$_{3n+1}$ ($n=1$ and 2) [16,18,33]. The Mn $3d$ magnetic moments in MnBi$_{2n}$Te$_{3n+1}$ form a long-range A-type AFM order below T_N, which breaks the time-reversal symmetry while the inversion symmetry is preserved. The theoretical calculations predict that MnBi$_{2n}$Te$_{3n+1}$ is also an axion insulator in the AFM phase, which is analogous to EuSn$_2$As$_2$ except for the large gap in the (001) SSs of MnBi$_{2n}$Te$_{3n+1}$ in the calculations [16,28,33]. To clarify the effects of the Mn $3d$ orbitals, especially on the topological SSs, we perform precise ARPES measurements on the (001) surface of MnBi$_{2n}$Te$_{3n+1}$ ($n=1$ and 2).

Figure 4 shows our synchrotron and laser ARPES data of MnBi$_2$Te$_4$. Compared with the previous ARPES results that exhibit a large gap of approximately 100 meV [21,25–27], our data reveal extra electronic states within the gap. In order to clarify the band dispersions of the in-gap states in the synchrotron ARPES data in Figs. 4(a) and 4(c), we perform a second derivative of the ARPES data with respect to energy. In the intensity maps of the second derivative in Figs. 4(b) and 4(d), two bands linearly cross, forming a Dirac point at -0.28 eV. The laser ARPES data in Figs. 4(f)–4(h) more clearly illustrate the Dirac-like band
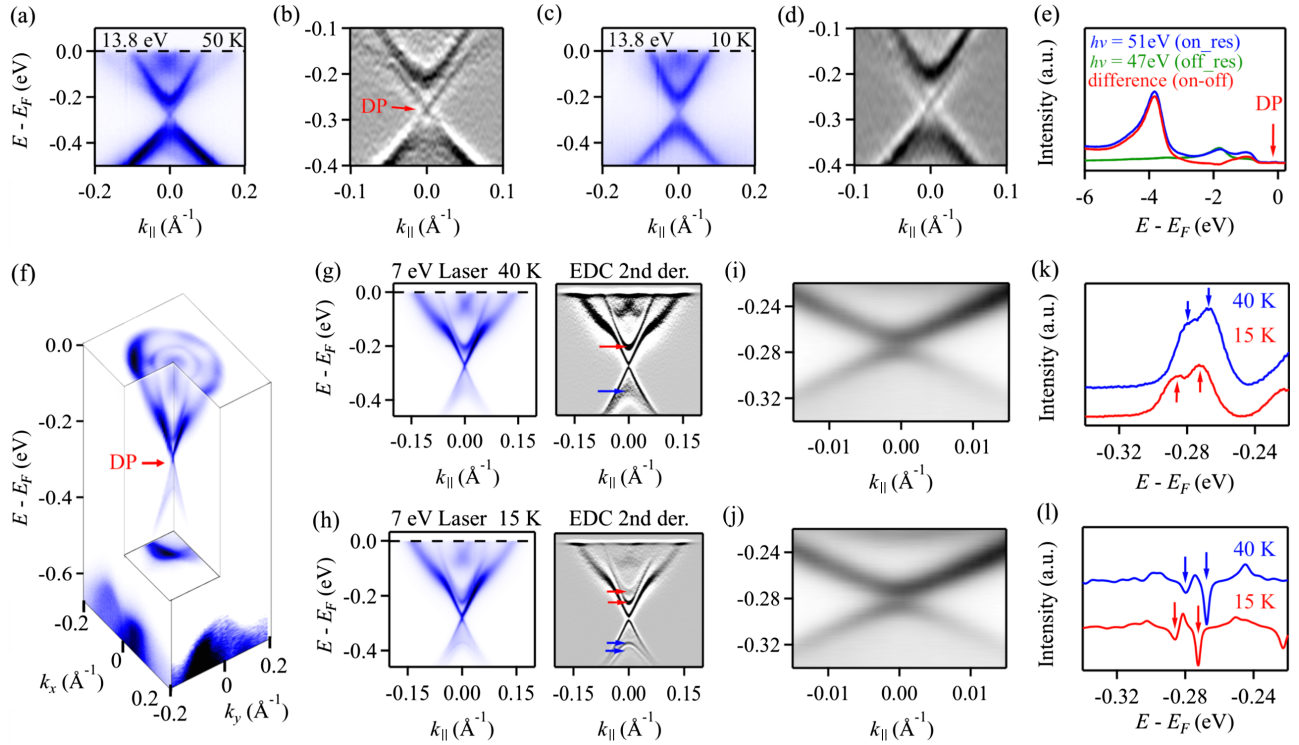
FIG. 4. Dirac SSs on the (001) surface of $MnBi_2Te_4$. (a),(c) ARPES intensity maps along the cut through $\bar{\Gamma}$ taken at $h\nu = 13.8$ eV at 50 and 10 K. (b),(d) Intensity maps of the second derivative with respect to the energy of the data near the bulk band gap in (a) and (c). DP is the abbreviation for Dirac point. (e) Resonant valence band spectra of $MnBi_2Te_4$ taken at the Mn $3p$-$3d$ absorption edge. On- and off-resonance spectra are obtained at $h\nu = 51$ and 47 eV, respectively. (f) Three-dimensional plot of the ARPES data around $\bar{\Gamma}$ taken with the 7-eV laser. (g),(h) ARPES intensity maps (left) and their second derivative with respect to the energy (right) along the cut through $\bar{\Gamma}$ taken with the 7-eV laser at 40 and 15 K. The red and blue arrows indicate splitting of the conduction and valance bands, respectively, below T_N. (i),(j) Enlarged ARPES intensity maps near the Dirac point in (g) and (h). (k) EDCs at $\bar{\Gamma}$ at 40 and 15 K. (l) Second derivative of the EDCs in (k).

dispersions of the SSs. Moreover, we observe splitting in the conduction and valence bands below T_N, which can be attributed to band folding along k_z and band reconstruction, as the long-range AFM order with an A-type magnetic structure leads to the doubling of the period along the c axis. By carefully examining the band dispersions near the Dirac point in Figs. 4(i) and 4(j), we reveal that the upper and lower branches of the Dirac SSs do not touch, corresponding to the double-peak structure of the energy distribution curves (EDCs) at $\bar{\Gamma}$ in Fig. 4(k) and their second-derivative spectra in Fig. 4(l).

Note that the gap exists in both PM and AF phases of $MnBi_2Te_4$ ($T_N = 24$ K). In Fig. 4(l), the second-derivative spectra of the EDCs at $\bar{\Gamma}$ determines that the gap is 12 meV at 40 K and 13.5 meV at 8 K. This difference is within the energy resolution ($\Delta E = 4.5$ meV) in the experiments, indicating that the AFM order has a quite small effect on the Dirac SSs. This result is in contrast to the theoretical calculations that propose that the Dirac SSs open an energy gap of tens of meV when $MnBi_2Te_4$ undergoes an AFM transition into the AFM-c phase [19–21,23,40]. The AFM-c phase in $MnBi_2Te_4$ has been confirmed by neutron diffraction experiments [35].

In $MnBi_2Te_4$, the magnetic moments derive from the Mn $3d$ states, and the nontrivial topology is caused by the inversion of the Bi $6p$ and Te $5p$ states near the bulk band gap. In order to clarify the contribution of magnetic Mn $3d$ states to the topological electronic states, we perform resonance photoemission spectroscopy measurements at the Mn $3p$-$3d$ absorption edge. The difference between the on- and off-resonance spectra in Fig. 4(e) reveals that the Mn $3d$ states are mainly located at approximately 4 eV below E_F. In addition, the feature at approximately 1 eV below E_F originates from the hybridization of the Mn $3d$ and Te $5p$ states. However, the component of Mn $3d$ states is negligible in the energy range within 0.6 eV below E_F, where the nontrivial topology arises. This result indicates that the hybridization of the Mn $3d$ states and the p orbitals related to the nontrivial topology is weak. The theoretical calculations may overestimate the effects of the magnetic order on the Dirac SSs even though the Mn $3d$ states are not as localized as the Eu $4f$ states. The inconsistency between the experiment and theory calls for further theoretical investigation.

We also reveal the existence of Dirac SSs within the large gap previously observed in $MnBi_4Te_7$ [28,29], as shown
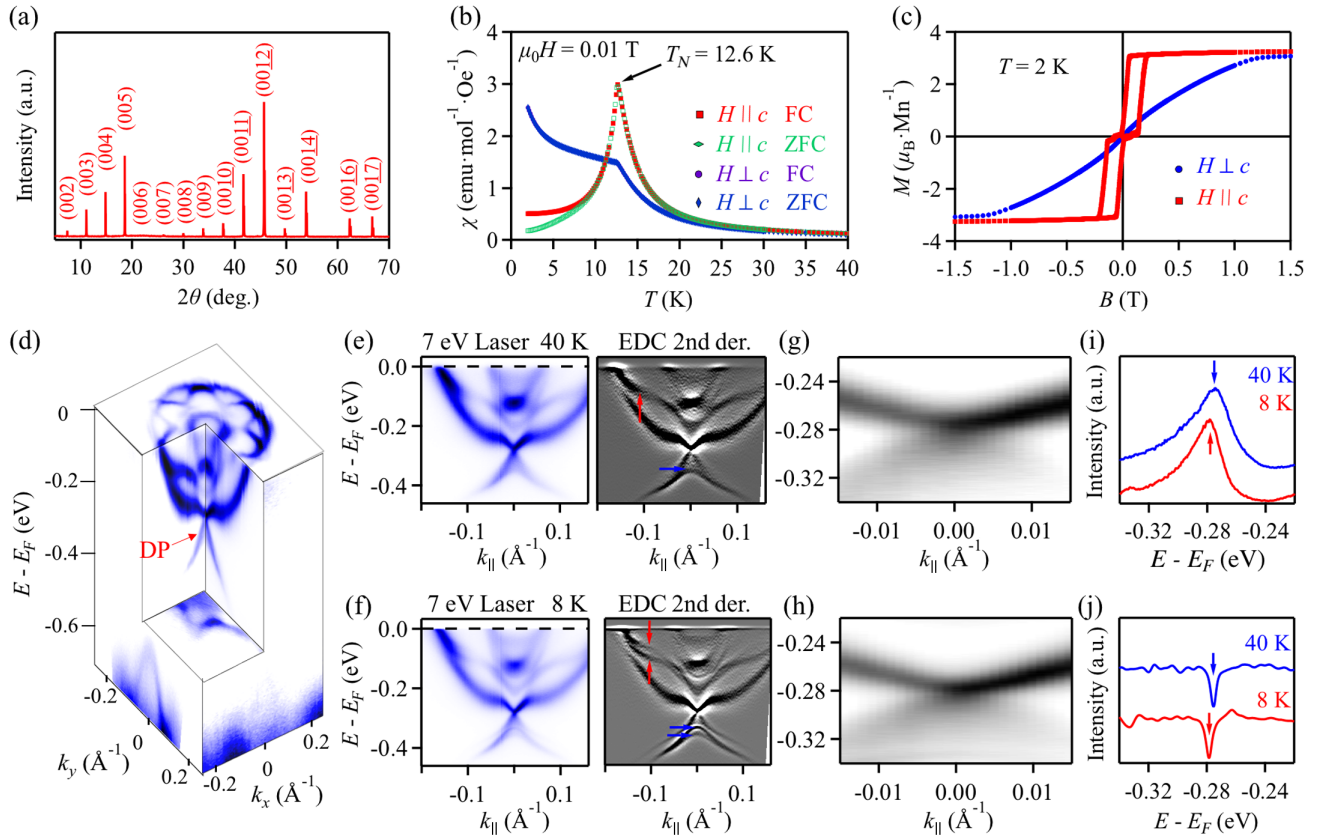
FIG. 5.   Dirac SSs on the (001) surface of $MnBi_4Te_7$. (a) X-ray diffraction pattern on the (001) surface of a $MnBi_4Te_7$ single crystal. (b) Temperature dependence of magnetic susceptibility $\chi(T)$ at magnetic field $\mu_0H = 0.01$ T parallel and perpendicular to the c axis under zero-field cooling (ZFC) and field cooling (FC). (c) Field-dependent magnetization $M(H)$ at 2 K with magnetic fields parallel (red line) and perpendicular (blue line) to the c axis. (d) Three-dimensional intensity plot of the ARPES data around $\bar{\Gamma}$ measured with the 7-eV laser. (e),(f) ARPES intensity maps (left) and their second derivative with respect to the energy (right) along the cut through $\bar{\Gamma}$ measured with the 7-eV laser at 40 and 8 K. The red and blue arrows indicate splitting of the conduction and valance bands, respectively, across T_N. (g),(h) Enlarged ARPES intensity maps near the Dirac point in (e) and (f). (i) EDCs at $\bar{\Gamma}$ measured at 40 and 8 K. (j) Second derivative of the EDCs in (i).

in Fig. 5. In the single crystal x-ray diffraction data in Fig. 5(a), all the peaks can be indexed by the (00l) reflections of $MnBi_4Te_7$ with $c = 23.811(2)$ Å, which is consistent with the previous results [36]. The magnetic susceptibility $\chi(T)$ in Fig. 5(b) with $H\|c$ shows a cusp at 12.6 K, which is an indication of an AFM transition consistent with the previous studies [28,29,43]. The isothermal magnetization $M(H)$ with $H\|c$ at 2 K in Fig. 5(c) exhibits a spin-flip transition, indicating that the magnetic moments are along the c axis in the AFM phase.

Figures 5(d)–5(f) show a Dirac-like band crossing at -0.28 eV at the $\bar{\Gamma}$ point within the bulk band gap. In Figs. 5(g) and 5(h), one can hardly recognize a gap at the Dirac point. The EDCs at $\bar{\Gamma}$ in Fig. 5(i) and their second-derivative spectra in Fig. 5(j) appear as a single-peak structure, which indicates that the gap is dramatically reduced from $MnBi_2Te_4$ to $MnBi_4Te_7$. A comparative study of them may help to clarify the origin of the gap in the PM

phase. The AFM ordering in $MnBi_4Te_7$ ($T_N = 12.6$ K) has little effect on the Dirac SS, indicating weak coupling between the magnetic Mn $3d$ states and the topological electronic states, which is similar to the case in $MnBi_2Te_4$.

It is expected on the (001) cleaved surface of $MnBi_4Te_7$ that there should be two kinds of termination [$MnBi_2Te_4$] and [Bi_2Te_3], which have different band dispersions of the surface states. However, we observe only one set of Dirac bands in the bulk band gap using the 7-eV laser. Our scanning tunneling microscopy measurements (not shown) confirm the existence of two different terminations on one cleaved surface. The sizes of each termination are typically less than 1×1 μm^2, which are much smaller than the spot size of the laser (approximately 50×50 μm^2). The absence of the other set of surface Dirac bands in our data is probably due to the matrix element effects. Systematic photon-energy-dependent measurements may reveal the other set of surface Dirac bands.

III. CONCLUSION

We observe the Dirac SSs across the bulk band gap of $EuSn_2As_2$ and $MnBi_{2n}Te_{3n+1}$ ($n = 1$ and 2), demonstrating their nontrivial topology. The Dirac SSs have almost no change when long-range AFM order develops in these materials, which can be attributed to weak coupling between the local magnetic moments and the topological electronic states. It is highly desirable to find the intrinsic magnetic TIs in that the topological electronic states are heavily involved in the magnetic order, which may be critical to realize topological quantum phenomena at higher temperatures.

IV. METHOD

A. Sample synthesis

Single crystals of $EuSn_2As_2$ are grown by the Sn flux method at the Institute of Physics, Chinese Academy of Sciences. The high-purity Eu (rod), Sn (shot), and As (lump) are put into corundum crucibles and sealed into quartz tubes with a ratio of $Eu:As:Sn = 1:3:20$. The tubes are heated to 1000°C at the rate of 100 °C/h, held there for 12 h, and then cooled to 750°C at a rate of 2°C/h. The flux is removed by centrifugation, and shiny crystals are obtained.

Both single crystals of $MnBi_2Te_4$ and $MnBi_4Te_7$ are grown by the self-flux method at Renmin University of China. The high-purity Mn (piece), Bi (shot), and Te (shot) are put into corundum crucibles and sealed into quartz tubes with a ratio of $Mn:Bi:Te = 1:11.7:18.55$ ($MnTe:Bi_2Te_3 = 1:5.85$) and $Mn:Bi:Te = 0.8:11.7:18.35$ ($MnTe:Bi_2Te_3 = 0.8:5.85$), respectively. The tube is heated to 950°C at a rate of 40°C/h, held there for 12 h, and then cooled to 585°C at a rate of 10°C/h. The flux is removed by centrifugation, and shiny crystals are obtained.

B. Band structure calculations

$EuSn_2As_2$ is crystallized in a rhombohedral lattice with space group of R-$3m$ (No. 166). The experimental lattice constants $a = b = 4.2071$ Å and $c = 26.463$ Å are adopted in our first-principles calculations. The Eu, Sn, and As atoms are located at the Wyckoff position $3a$ (0, 0, 0), $6c$ (0, 0, 0.20963), and $6c$ (0, 0, 0.40624), respectively. The Vienna *Ab initio* Simulation Package (VASP) with the generalized gradient approximation–Perdew, Burke, and Ernzerhof (PBE–GGA)-type exchange correlation potential is employed, and the BZ sampling is performed by using k grids with an $11 \times 11 \times 3$ mesh in self-consistent calculations. To match the energy position of Eu $4f$ bands in the experiments, the Hubbard U parameter of the $4f$ electrons is taken as 5 eV in the $GGA + U$ calculations. We generate the maximally localized Wannier functions for the $5s$ and $5p$ orbitals on Sn and the $4p$ orbitals on As using the WANNIER90 package. The surface state calculations are performed using the Green's function method based on the Wannier Tools package.

C. Synchrotron and laser angle-resolved photoemission spectroscopy

Synchrotron ARPES measurements on $EuSn_2As_2$ are performed at the "CASSIOPEE" beam line, SOLEIL, France, with a Scienta R4000 analyzer, and the "dreamline" beam line at the Shanghai Synchrotron Radiation Facility (SSRF) with a Scienta DA30 analyzer. Synchrotron ARPES measurements on $MnBi_2Te_4$ are performed at the 03U beam line at the SSRF and at the 13U beam line at the National Synchrotron Radiation Laboratory at Hefei with a Scienta DA30 analyzer. High-resolution ARPES measurements on $MnBi_2Te_4$ and $MnBi_4Te_7$ are performed using the 7-eV laser ARPES at the Institute of Solid Physics, University of Tokyo with a Scienta R4000 analyzer.

D. Time-resolved angle-resolved photoemission spectroscopy

The tr-ARPES experiments are performed at Shanghai Jiao Tong University. In tr-ARPES measurements, infrared photon pulses with a wavelength centered at 700 nm (1.77 eV) and a pulse length of 30 fs are used to excite the sample, and the nonequilibrium states are probed by ultraviolet pulses at 205 nm (6.05 eV). Photoelectrons are collected by a Scienta DA30L-8000R analyzer. The overall time resolution and energy resolution are 130 fs and 19 meV, respectively [44]. The sample is cleaved at a pressure better than 3×10^{-11} torr at 4 K.

Note added.—Recently, we became aware of similar studies in Refs. [45–47] and the updated version of Ref. [26] showing the Dirac SSs in MnBi$_2$Te$_4$.

[1] K. v. Klitzing, G. Dorda, and M. Peper, *New Method for High-Accuracy Determination of the Fine-Structure Constant Based on Quantized Hall Resistance*, Phys. Rev. Lett. **45**, 494 (1980).

[2] D. J. Thouless, M. Kohmoto, M. P. Nightingale, and M. den Nijs, *Quantized Hall Conductance in a Two-Dimensional Periodic Potential*, Phys. Rev. Lett. **49**, 405 (1982).

[3] F. D. M. Haldane, *Fractional Quantization of the Hall Effect: A Hierarchy of Incompressible Quantum Fluid States*, Phys. Rev. Lett. **51**, 605 (1983).

[4] F. D. M. Haldane, *Model for a Quantum Hall Effect without Landau Levels: Condensed-Matter Realization of the "Parity Anomaly"*, Phys. Rev. Lett. **61**, 2015 (1988).

[5] S. Murakami, N. Nagaosa, and S.-C. Zhang, *Spin-Hall Insulator*, Phys. Rev. Lett. **93**, 156804 (2004).

[6] C. L. Kane and E. J. Mele, *Z_2 Topological Order and the Quantum Spin Hall Effect*, Phys. Rev. Lett. **95**, 146802 (2005).

[7] L. Fu and C. L. Kane, *Topological Insulators with Inversion Symmetry*, Phys. Rev. B **76**, 045302 (2007).

[8] R. S. K. Mong, A. M. Essin, and J. E. Moore, *Antiferromagnetic Topological Insulators*, Phys. Rev. B **81**, 245209 (2010).

[9] R. Yu, W. Zhang, H. J. Zhang, S. C. Zhang, X. Dai, and Zhong Fang, *Quantized Anomalous Hall Effect in Magnetic Topological Insulators*, Science **329**, 61 (2010).

[10] C.-Z. Chang et al., *Experimental Observation of the Quantum Anomalous Hall Effect in a Magnetic Topological Insulator*, Science **340**, 167 (2013).

[11] J. Wang, B. Lian, and S.-C. Zhang, *Quantum Anomalous Hall Effect in Magnetic Topological Insulators*, Phys. Scr. T **T164**, 014003 (2015).

[12] J. G. Checkelsky, R. Yoshimi, A. Tsukazaki, K. S. Takahashi, Y. Kozoka, J. Falson, M. Kawasaki, and Y. Tokura, *Trajectory of the Anomalous Hall Effect towards the Quantized State in a Ferromagnetic Topological Insulator*, Nat. Phys. **10**, 731 (2014).

[13] X.-F. Kou et al., *Scale-Invariant Quantum Anomalous Hall Effect in Magnetic Topological Insulators beyond the Two-Dimensional Limit*, Phys. Rev. Lett. **113**, 137201 (2014).

[14] C.-Z. Chang, W.-W. Zhao, D. Y. Kim, H.-J. Zhang, B. A. Assaf, D. Heiman, S.-C. Zhang, C.-X. Liu, M. H. W. Chan, and J. S. Moodera, *High-Precision Realization of Robust Quantum Anomalous Hall State in a Hard Ferromagnetic Topological Insulator*, Nat. Mater. **14**, 473 (2015).

[15] M. Mogi, M. Kawamura, R. Yoshimi, A. Tsukazaki, Y. Kozuka, N. Shirakawa, K. S. Takahashi, M. Kawasaki, and Y. Tokura, *A Magnetic Heterostructure of Topological Insulators as a Candidate for an Axion Insulator*, Nat. Mater. **16**, 516 (2017).

[16] D.-Q. Zhang, M.-J. Shi, T.-S. Zhu, D.-Y. Xing, H.-J. Zhang, and J. Wang, *Topological Axion States in Magnetic Insulator MnBi$_2$Te$_4$ with the Quantized Magnetoelectric Effect*, Phys. Rev. Lett. **122**, 206401 (2019).

[17] Y.-F. Xu, Z.-D. Song, Z.-J. Wang, H.-M. Weng, and X. Dai, *Higher-Order Topology of the Axion Insulator EuIn$_2$As$_2$*, Phys. Rev. Lett. **122**, 256402 (2019).

[18] Y. Gong et al., *Experimental Realization of an Intrinsic Magnetic Topological Insulator*, Chin. Phys. Lett. **36**, 076801 (2019).

[19] J.-H. Li, C. Wang, Z.-T. Zhang, B.-L. Gu, W.-H. Duan, and Y. Xu, *Magnetically Controllable Topological Quantum Phase Transitions in Antiferromagnetic Topological Insulator MnBi$_2$Te$_4$*, Phys. Rev. B **100**, 121103(R) (2019).

[20] M. M. Otrokov, I. P. Rusinov, M. Blanco-Rey, M. Hoffman, A. Yu. Vyazovskaya, S. V. Eremeev, A. Ernst, P. M. Echenique, A. Arnau, and E. V. Chulkov, *Unique Thickness-Dependent Properties of the van der Waals Interlayer Antiferromagnet MnBi$_2$Te$_4$ Films*, Phys. Rev. Lett. **122**, 107202 (2019).

[21] M. M. Otrokov et al., *Prediction and Observation of the First Antiferromagnetic Topological Insulator*, arXiv:1809.07389.

[22] X.-L. Qi, T. L. Hughes, and S.-C. Zhang, *Chiral Topological Superconductor from the Quantum Hall State*, Phys. Rev. B **82**, 184516 (2010).

[23] H.-Y. Sun, B.-W. Xia, Z.-J. Chen, Y.-J. Zhang, P.-F. Liu, Q.-S. Yao, H. Tang, Y.-J. Zhao, H. Xu, and Q.-H. Liu, *Rational Design Principles of Quantum Anomalous Hall Effect from Superlattice-like Magnetic Topological Insulators*, Phys. Rev. Lett. **123**, 096401 (2019).

[24] X. Gui et al., *A New Magnetic Topological Quantum Material Candidate by Design*, arXiv:1903.03888.

[25] R. C. Vidal et al., *Surface States and Rashiba-Type Spin Polarization in Antiferromagnet MnBi$_2$Te$_4$ (0001)*, Phys. Rev. B **100**, 121104(R) (2019).

[26] B. Chen et al., *Searching the Mn(Sb, Bi)$_2$Te$_4$ Family of Materials for the Ideal Intrinsic Magnetic Topological Insulator*, Nat. Commun. **10**, 4469 (2019).

[27] S. H. Lee et al., *Spin Scattering and Noncollinear Spin Structure-Induced Intrinsic Anomalous Hall Effect in Antiferromagnetic Topological Insulator MnBi$_2$Te$_4$*, Phys. Rev. Res. **1**, 012011(R) (2019).

[28] C.-W. Hu et al., *A van der Waals Antiferromagnetic Topological Insulator with Weak Interlayer Magnetic Coupling*, arXiv:1905.02154.

[29] J.-Z. Wu, F.-C. Liu, M. Sasase, K. Ienaga, Y. Obata, R. Yukawa, K. Horiba, H. Kumigashira, S. Okuma, T. Inoshita, and H. Hosono, *Natural van der Waals Heterostructures with Tunable Magnetic and Topological States*, arXiv:1905.02385.

[30] Y.-J. Deng, Y.-J. Yu, M.-Z. Shi, J. Wang, X.-H. Chen, and Y.-B. Zhang, *Magnetic-Field-Induced Quantized Anomalous Hall Effect in Intrinsic Magnetic Topological Insulator MnBi$_2$Te$_4$*, arXiv:1904.11468.

[31] S. Zhang et al., *Experimental Observation of the Gate-Controlled Reversal of the Anomalous Hall Effect in the*

Intrinsic Magnetic Topological Insulator $MnBi_2Te_4$ *Device*, arXiv:1905.04839.

[32] C. Liu, Y.-C. Wang, H. Li, Y. Wu, Y.-X. Li, J.-H. Li, K. He, Y. Xu, J.-S. Zhang, and Y.-Y. Wang, *Quantum Phase Transition from Axion Insulator to Chern Insulator in* $MnBi_2Te_4$, arXiv:1905.00715.

[33] J.-H. Li, Y. Li, S.-Q. Du, Z. Wang, B.-L. Gu, S.-C. Zhang, K. He, W.-H. Duan, and Y. Xu, *Intrinsic Magnetic Topological Insulators in van der Waals Layered* $MnBi_2Te_4$-*Family Materials*, Sci. Adv. **5**, eaaw5685 (2019).

[34] J.-H. Cui, M.-Z. Shi, H.-H. Wang, F.-H. Yu, T. Wu, X.-G. Luo, J.-J. Ying, and X.-H. Chen, *Transport Properties of Thin Flakes of the Antiferromagnetic Topological Insulator* $MnBi_2Te_4$, Phys. Rev. B **99**, 155125 (2019).

[35] J.-Q. Yan, Q. Zhang, T. Heitmann, Z.-L. Huang, K.-Y. Chen, J.-G. Cheng, W.-D. Wu, D. Vaknin, B. C. Sales, and R. J. McQueeney, *Crystal Growth and Magnetic Structure of* $MnBi_2Te_4$, Phys. Rev. Mater. **3**, 064202 (2019).

[36] P. Rani, A. Saxena, R. Sultana, V. Nagpal, S. S. Islam, S. Patnaik, and V. P. S. Awana, *Crystal Growth and Basic Transport and Magnetic Properties of* $MnBi_2Te_4$, arXiv:1906.09038.

[37] A. Zeugner *et al.*, *Chemical Aspects of the Antiferromagnetic Topological Insulator* $MnBi_2Te_4$, Chem. Mater. **31**, 2795 (2019).

[38] J.-Q. Yan, S. Okamoto, M. A. McGuire, A. F. May, R. J. McQueeney, and B. C. Sales, *Evolution of Structural, Magnetic and Transport Properties in* $MnBi_{2-x}Sb_xTe_4$, Phys. Rev. B **100**, 104409 (2019).

[39] K.-Y. Chen, B.-S. Wang, J.-Q. Yan, D. S. Parker, J.-S. Zhou, Y. Uwatoko, and J.-G. Cheng, *Suppression of the Antiferromagnetic Metallic State in the Pressurized* $MnBi_2Te_4$ *Single Crystal*, Phys. Rev. Mater. **3**, 094201 (2019).

[40] M. M. Otrokov, T. V. Menshchikova, I. P. Rusinov, M. G. Vergniory, V. M. Kuznetsov, and E. V. Chulkov, *Magnetic Extension as an Efficient Method for Realizing the Quantum Anomalous Hall State in Topological Insulators*, JETP Lett. **105**, 297 (2017).

[41] M. Q. Arguilla, N. D. Cultrara, Z. J. Baum, S. Jiang, R. D. Ross, and J. E. Goldberger, $EuSn_2As_2$: *An Exfoliatable Magnetic Layered Zintl-Klemm Phase*, Inorg. Chem. Front. **4**, 378 (2016).

[42] L. Fu and C. L. Kane, *Topological Insulators with Inversion Symmetry*, Phys. Rev. B **76**, 045302 (2007).

[43] D. Souchay *et al.*, *Layered Manganese Bismuth Tellurides with* $GeBi_4Te_7$- *and* $GeBi_6Te_{10}$-*Type Structures: Towards Multifunctional Materials*, J. Mater. Chem. C **7**, 9939 (2019).

[44] Y.-Y. Yang, T.-W. Tang, S.-F. Duan, C.-C. Zhou, D.-X. Hao, and W.-T. Zhang, *A Time- and Angle-Resolved Photoemission Spectroscopy with Probe Photon Energy up to 6.7 eV*, Rev. Sci. Instrum. **90**, 063905 (2019).

[45] Y.-J. Hao *et al.*, preceding paper, *Gapless Surface Dirac Cone in Antiferromagnetic Topological Insulator* $MnBi_2Te_4$, Phys. Rev. X **9**, 041038 (2019).

[46] Y. J. Chen *et al.*, following paper, *Topological Electronic Structure and Its Temperature Evolution in Antiferromagnetic Topological Insulator* $MnBi_2Te_4$, Phys. Rev. X **9**, 041040 (2019).

[47] P. Swatek, Y. Wu, L.-L. Wang, K. Lee, B. Schrunk, J.-Q. Yan, and A. Kaminski, *Gapless Dirac Surface States in the Antiferromagnetic Topological Insulator* $MnBi_2Te_4$, arXiv:1907.09596.

Correction: Section headings in the middle of the paper were missing and have been inserted.